# Effects of the Floating Capacitor Voltage on the Torque-Speed Characteristic of an Open-End Winding Synchronous Reluctance Motor Drive

Jacopo Riccio, *Member, IEEE*, Filippo Gemma, *Student Member, IEEE*, Luca Rovere, *Member, IEEE*, Giulia Tresca, *Member, IEEE*, Mauro Di Nardo *Member, IEEE*, Shafiq Odhano *Member, IEEE*, Michele Degano, *Senior Member, IEEE*, Pericle Zanchetta, *Fellow, IEEE*.

***Abstract*—This manuscript investigates the torque-speed characteristics of a synchronous reluctance motor drive with an open-end winding (OEW) configuration. The machine is powered by standard two-level voltage source inverters (VSI), one supplied by a DC power source while the other connected to a floating capacitor (FC). The analysis considers the flux maps of a synchronous reluctance motor identified through experiments to account for the effect of the self-and cross-saturation phenomenon. The study reveals that the dual-inverter (DI) configuration with a FC can significantly extend the constant torque speed range and achieve unity power factor. In addition, the analysis demonstrates that the torque in the constant power speed range can be noticeably increased compared to the standard single-inverter (SI) configuration. With the full model of the OEW drive plant, the FC voltage can be purposefully selected to modify the drive torque speed characteristic to benefit the specific application. The advantages of the investigated synchronous drive architecture have been experimentally validated in different operating conditions with a purposely built set-up.**

***Index Terms*—Open-End Winding, Two-Level Inverter, Dual-Inverter, Synchronous Reluctance Motor Drive, Floating Capacitor, Torque-Speed, Power Factor, Field-Weakening.**

## I. Introduction

Synchronous reluctance (SyRel) motor drives are a compelling alternatives to induction and permanent magnet synchronous motor drives in a wide spectrum of applications [1]. This broad application uptake can be attributed to their high dynamic performance, good power density, competitive costs, and reduced environmental impact due to the lack of rare earth permanent magnet materials [2]. Despite their cost-effectiveness, SyRel motor drives have significant drawbacks such as low power factor and constant power speed range, high torque ripple, and the highly non-linear magnetic behaviour which greatly complicates the control structure.

Jacopo Riccio, Luca Rovere and Michele Degano are with the Department of Electrical and Electronic Engineering, University of Nottingham, Nottingham, UK; e-mail:Jacopo.Riccio2@nottingham.ac.uk, Luca.Rovere@nottingham.ac.uk, michele.degano@nottingham.ac.uk

Filippo Gemma, Giulia Tresca and Pericle Zanchetta are with Electrical, Computer and Biomedical Engineering Dept., Pavia, Italy; e-mail: filippo.gemma01@universitadipavia.it, giulia.tresca01@universitadipavia.it, pericle.zanchetta@unipv.it

Mauro Di Nardo is with Department of Electrical and Information Engineering, Politecnico di Bari, Bari, Italy; e-mail: mauro.dinardo@poliba.it

Shafiq Odhano is with the School of Engineering, Newcastle University, Newcastle Upon Tyne, UK; e-mail: shafiq.odhano@newcastle.ac.uk

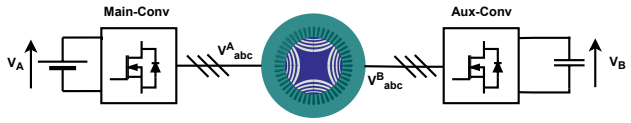


Fig. 1: SyRel in OEW with FC drive scheme.

The standard engineering solution to tackle both low power factor and narrow constant power speed range challenges is to add permanent magnets within the rotor flux barriers [3]. Despite being effective, this approach requires a significant amount of rare-earth based-PM assistance, especially when a high overload is required as in traction applications [4]. The use of PMs does obviously not guarantee stability of the supply chain in the current market ecosystem where sudden shortages or rapid price fluctuation of rare-earth elements are possible.

Another promising approach aimed at extending the constant power speed range and increasing the power factor of SyRel drives involves the adoption of a SyRel machine with an open-end winding (OEW) configuration where each side is supplied by a three phase voltage source inverter [5], [6]. This configuration allows to increase the voltage applied at the motor terminals and exploit the intrinsic multilevel voltage output capability, offering improved control of both torque and speed. Furthermore, the OEW design contributes to improved fault tolerance [7] as it allows the machine to keep running by redirecting the current through unaffected sections. These features collectively enhance the overall reliability and robustness of the motor drive system.

Fig. 1 depicts the described system where both ends of the machine's windings are supplied with a main converter (Main-Conv) and an auxiliary converter (Aux-Conv). Three distinct configurations have been proposed in literature differing according to the way the DC-link auxiliary converter is connected: 1) a common DC-link shared between the two inverters [8], [9]; 2) two isolated DC-links independently supplied [10], [11]; 3) the DC-link of the Aux-Conv is connected to a floating capacitor (FC) [12], [13].

While the common DC-bus topology offers advantages such as a compact design, a high torque per volume ratio, and fault tolerance, challenges arise due to the presence of zero-sequence current [14]. Either the converter's output Common

Mode Voltage is eliminated by employing a more complex modulation strategy and reduced input/output voltage transfer ratio or additional system losses and increased torque ripple have to be accepted [15]. The two isolated DC-link solution helps avoid zero-sequence current circulation. However, as for the standard VSIs, the common-mode voltage generated by the stand-alone DC buses can cause shaft voltage and bearing current which can reduce the drive's useful life [16]. In the FC solution, zero-sequence current circulation problem is not present [13] and has the additional advantage that the FC voltage level can be adjusted during the motor operation to enhance torque-versus-speed characteristic [12]. Indeed, by setting a relatively large FC voltage extends the constant-torque region and delays the onset of field weakening operations. The voltage ratio between the two DC buses plays a crucial role in determining DC-link voltage utilization and torque-versus-speed characteristics. Existing studies have primarily focused on extending the performance of the torque-speed curve by relaxing the power factor constraint in induction motors [17], [18], or in analyzing single voltage ratios [19], [20], but the full potential of selecting the FC voltage level to enhance drive performance for a SyRel motor remains largely unexplored.

This paper attempts to fill this gap by exploring the performance of a SyRel drive with an OEW configuration with a FC in order to increase the constant torque region without altering the internal characteristics of the machine.

This manuscript is based on [21], and investigates how the torque-versus-speed performance are affected by the FC voltage considering the non-linear magnetic behaviour of the commercially available SyRel machine. The paper is structured as follows: Section II introduces the magnetic model experimental characterization and the motor operations with a single inverter supply. Then, the linear OEW SyRel motor operations are discussed in Section III, while Section IV covers the real OEW SyRel motor operations. Section V presents the experimental results and Section VI discusses the advantages of the DI configuration. Finally, Section VII concludes the paper by summarizing key findings and suggesting future directions.

## II. Magnetic Model Experimental Characterization and SI Drive Operations

The defining equations of a SyRel machine can be expressed in the $dq$ rotating reference frame as follows [22]:

$$\begin{cases} v_d = R_s i_d \ + \ L_d \frac{di_d}{dt} \ - \ w_r i_q L_q \\ v_q = R_s i_q \ + \ L_q \frac{di_q}{dt} \ + \ w_r i_d L_d \end{cases} \tag{1}$$

$$\begin{cases} L_d\left(i_d, i_q\right) = \frac{\phi_d(i_d, i_q)}{i_d} \\ L_q\left(i_d, i_q\right) = \frac{\phi_q(i_d, i_q)}{i_q} \end{cases} \tag{2}$$

$$T_{em} = \frac{3}{2} p \left(\phi_d i_q - \phi_q i_d\right) \tag{3}$$

where $L_d$, $L_q$, $\phi_d$, $\phi_q$, $i_d$ and $i_q$ are the $d$- and $q$-axis inductances, flux and currents, respectively; $v_d$ and $v_q$ are the $dq$ stator voltages, while $T_{em}$ is the electromagnetic torque; $\omega_r$ is the rotor electrical speed, $R_s$ is the stator resistance, and $p$ is the number of pole pairs.

| Variable | Symbol | Value | Unit |
|---|---|---|---|
| Stator Resistance | $R_s$ | 6.3 | Ω |
| Rated Torque | $T_{em}$ | 7 | Nm |
| Rated Speed | $\omega_m$ | 1500 | rpm |
| Rated Power | $P_n$ | 1.1 | kW |
| Rated Current (RMS) | $I_n$ | 2.9 | A |
| Rated Voltage (RMS) | $V_n$ | 380 | V |
| Pole Pairs | $p$ | 2 | # |

TABLE I: SyRel motor under test: nameplate.

A distinguishing feature of the SyRel resides in the non-linear flux versus current characteristics due to the self-axis and cross-saturation phenomena [22]. The self-axis saturation shows that direct and quadrature current components saturate the direct and quadrature flux components, respectively. The cross-saturation consists of direct-flux variations due to changes in quadrature current and vice versa. As a result, the $d$- and $q$-flux components have to be considered as non-linear functions of the current vector (i.e. $\phi_d(i_d, i_q)$, $\phi_q(i_d, i_q)$).

One of the most acknowledged procedures to identify the flux-versus-current maps of the SyRel motor is the one reported in [23], and it will be here carried out to identify the aforementioned $\phi_d$, $\phi_q$ characteristics. The test rig is shown in Fig. 2. It consists of a prime mover (PM) coupled to the SyRel motor under test whose characteristics are reported in Tab. I. The experimental tests consist of setting the PM rotational speed while the SyRel operate as a load in current control mode in several operable points in the $d$- and $q$-current domain.

The identified $\phi_d$ and $\phi_q$ characteristics are reported in Fig. 3(a) and 3(b). In the same figure, the linear magnetic characteristics are also highlighted. From the given flux maps, the calculated ideal and experimental electromagnetic torque represented by $T_{em}$ is reported in Fig. 4(a) and 4(b), respectively. In addition, the resulting apparent inductance on both $d$- and $q$-axis represented as non-linear function of the $d$- and $q$-axis current are represented in Fig. 5(a) and 5(b), respectively.

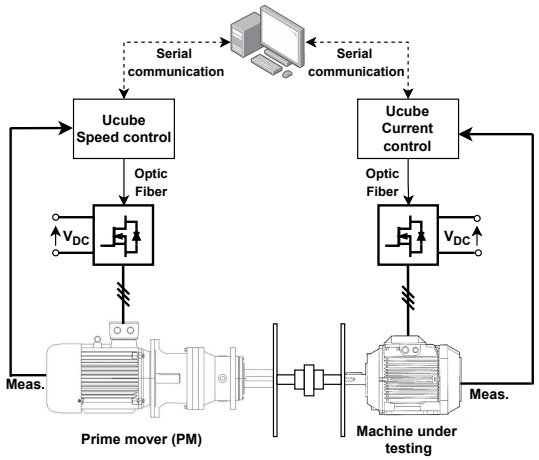


Fig. 2: Schematic hardware setup for magnetic characterization.

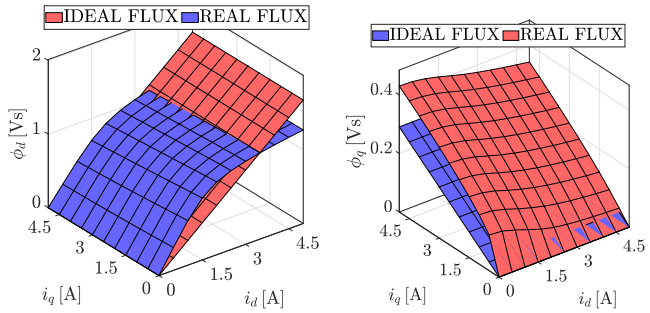


Fig. 3: Flux maps experimental results: (a) $d$-flux and (b) $q$-flux magnetic characteristics.

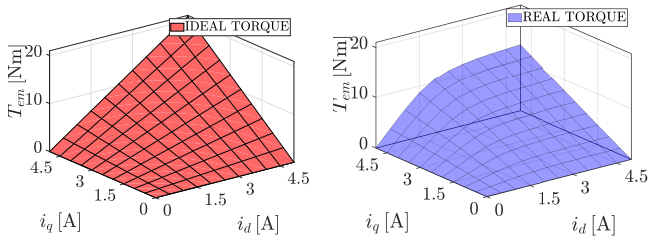


Fig. 4: Electromagnetic torque: (a) ideal, (b) experimental.

The knowledge of the flux and torque maps in the dq current plane allows to derive the control loci of a SyRel drive system with SI configuration with a 2-level VSI connected to the stator and powered by a fixed DC voltage source. The assumptions to derive such loci include negligible stator resistance, iron losses, and ideal converter switching behavior. Target values are detailed in Tab. I, with optimal trajectories extracted numerically. Maximum torque per ampere (MTPA) and maximum torque per watt (MTPW) are evaluated using isotorque curves, as shown in Fig. 6(a).

Three operating regions are identified: constant torque region (CTR) operates below base speed ($w_b^{SI} = 1500$ rpm). Fig. 6(b) illustrates torque-versus-speed characteristics, showing maximum torque in CTR and decreasing torque during flux-weakening. Second flux-weakening region (SFWR) is introduced to reduce torque loss at high speeds, with the transition marked by the depowering speed. In this region, the current vector follows the MTPW trajectory.

## III. Ideal OEW SyRel Motor Operations

The analytical model of an OEW SyRel drive system is hereafter presented to identify the impact of the floating capacitor voltage level on the resulting torque versus speed characteristics. The schematic drive system topology is depicted in Fig. 1. The study has been carried out at a steady state considering the $dq$ coordinates synchronous with the SyRel current, assuming 1) negligible stator resistance; 2) linear magnetic characteristics (i.e. $\overline{L}_d$, $\overline{L}_q$); 3) ideal switching behavior of the converters; and 4) iron losses neglected. In addition, the rated voltage as reported in Tab. I was considered hereafter to set the main converter (main-conv) DC link

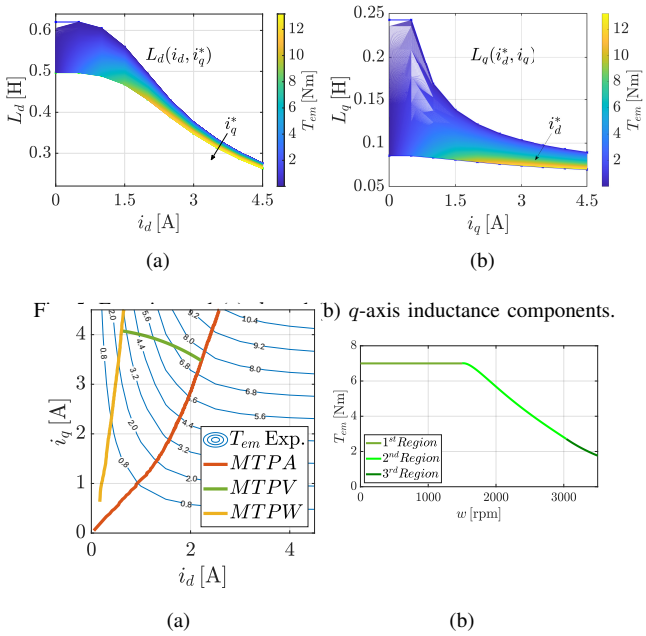


Fig. 6: Experimental (a) id,iq-plane Real SI MTPA, maximum torque per voltage (MTPV), MTPW trajectories for the machine under testing. (b) Torque-versus-speed characteristic real SI configuration.

voltage. Referring to the DC-side reactive power (i.e. $Q_A$) and the FC-side active power (i.e. $P_B$), the following conditions can be imposed:

$$Q_A = \frac{3}{2}\left(v_{Aq} i_d - v_{Ad} i_q\right) = \bar{Q} \tag{4a}$$

$$P_B = \frac{3}{2}\left(v_{Bd} i_d + v_{Bq} i_q\right) = 0 \tag{4b}$$

where the DC- and the FC-side voltages are denoted by $v_{Ad}$, $v_{Aq}$, $v_{Bd}$, $v_{Bq}$, respectively.

The constraint $P_B = 0$ is essential to keep the capacitor voltage constant. On the other hand, $\bar{Q}$ is a designer's choice set to compensate a specific amount of the reactive power of the machine. The unity power factor constraint set by $Q_A = 0$ in (4) is a designer choice, which is particularly beneficial for low power factor motors such as the SyRel considered in this work. The SyRel stator voltage equation can be represented in the $dq$ frame (i.e. $v_d$, $v_q$) at steady state as follows:

$$v_d = v_{Ad} - v_{Bd} = -w_r i_q \overline{L}_q \tag{5a}$$

$$v_q = v_{Aq} - v_{Bq} = +w_r i_d \overline{L}_d \tag{5b}$$

Combining (4) and (5) yields the magnitudes of the resulting voltage vectors:

$$|v_A| = \omega_r \frac{i_q i_d \left(\overline{L}_d - \overline{L}_q\right)}{\sqrt{i_d^2 + i_q^2}} \tag{6}$$

$$|v_B| = \omega_r \frac{\overline{L}_d i_d^2 + \overline{L}_q i_q^2}{\sqrt{i_d^2 + i_q^2}} \tag{7}$$

In general, the lowercase letter, $|v_{A,B}|$, is used to represent the magnitude, while the capital letter, $V_{A,B}$, denotes the set-point value for that case.

Depending on the magnitudes of $|v_A|$ and $|v_B|$, along with the chosen trajectory of the current vector, three distinct operating regions can be distinguished. The initial region, labeled as 'Region A', is characterized by both sides' voltages remaining unsaturated, with the drive operating below the base speed ($w_b^{DI}$). Once that $w_b^{DI}$ is exceeded, the drive enters the first flux-weakening region known as 'Region B'. The current vector follows a trajectory on the current circle limit and one of the two inverters' DC-links is saturated. During the flux weakening, the electromagnetic torque decreases as the rotational speed increases. To prevent excessive torque reduction at high rotational speeds, the current magnitude can be reduced at a fixed current angle, marking the second flux-weakening region, called 'Region C'. The rotational speed at which the transition occurs from 'Region B' to 'Region C' is commonly referred to as the depowering speed ($w_{dp}^{DI}$).

In the first operational region, the current vector is chosen along the optimal MTPA trajectory within the current plane (i.e. $i_d = i_q$), as illustrated in Fig.s 7(a) and 7(b). Combining the MTPA trajectory, equations (6) and (7), the $w_b^{DI}$ can be determined as follows [21]:

$$w_b^{DI} = min\left\{ w_A = \frac{2\,|v_A|}{I_n\,(\overline{L}_d - \overline{L}_q)}\ ,\ w_B = \frac{2\,|v_B|}{I_n\,(\overline{L}_d + \overline{L}_q)} \right\} \quad (8)$$

where $I_n$ represents the maximum current as a thermal limit for the drive (minimum among converter and motor), and $w_b^{DI}$ is evaluated based on which side the voltage source reaches the saturation target first. Comparing $w_b^{DI}$ with the one of the SI (i.e. $w_b^{SI} = \frac{\sqrt{2}V_n}{I_n\sqrt{\overline{L}_d^2+\overline{L}_q^2}}$), the following expression can be derived:

$$|v_A| \geq \frac{\sqrt{2}\,(\overline{L}_d + \overline{L}_q)}{2\sqrt{\overline{L}_d^2 + \overline{L}_q^2}} V_n \quad |v_B| \geq \frac{\sqrt{2}\,(\overline{L}_d - \overline{L}_q)}{2\sqrt{\overline{L}_d^2 + \overline{L}_q^2}} V_n \quad (9)$$

where $V_n$ denotes the rated voltage of the SyRel motor.

From (9), it can be deduced that $w_b^{DI}$ will be higher compared to the one of the SI (i.e. $w_b^{SI} = 1500$ rpm). Moreover, (9) suggests that the same base speed as the SI configuration can be always achieved in a DI configuration for lower voltage levels, given the inherent nature of the SyRel motor characterized by $\overline{L}_d > \overline{L}_q$. In fact, if the FC voltage is set to zero, the motor operates with the stator windings connected together to create a neutral point as for the standard SI configuration.

The drive enters in the second operation region, the first flux weakening region, with either $|v_A|$ or $|v_B|$ voltages saturated. In order to determine the speed-torque FC DI drive profile, the magnitude of the motor voltages $|v_A|$ and $|v_B|$ must be evaluated to observe which one saturates first then entering the first flux weakening region. In order to identify the upper rotational speed boundary of this region, two approaches have to be distinguished for the ideal OEW configuration [21]: one consists of taking into account the maximum torque per flux trajectory (MTPF), while the second one consists of evaluating the rotational speed at which both, the DC-link voltage of the Main-Conv, and the FC of the Aux-Conv saturate. $w_{dp}^{DI}$ is

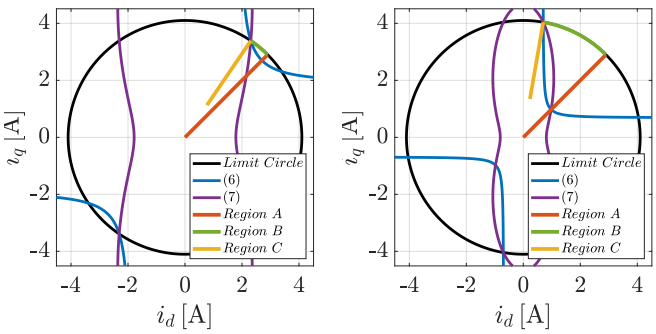


(a) (b)

Fig. 7: (a) Case 1: id,iq-plane ideal DI trajectories for $VB = 351$ V. (b) Case 2: id,iq-plane ideal DI trajectories for $VB = 290$ V.

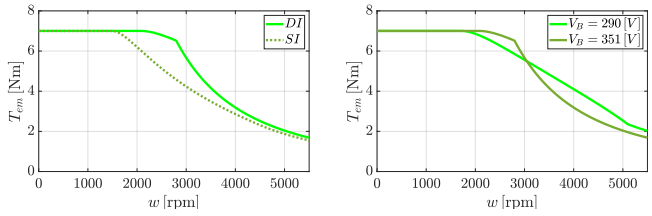


(a) (b)

Fig. 8: (a) Case 1: Torque-versus-speed characteristic ideal DI for $VB = 351$ V and SI configuration. (b) Case 2: Torque-versus-speed characteristic ideal DI for $VB = 290$ V and $VB = 351$ V.

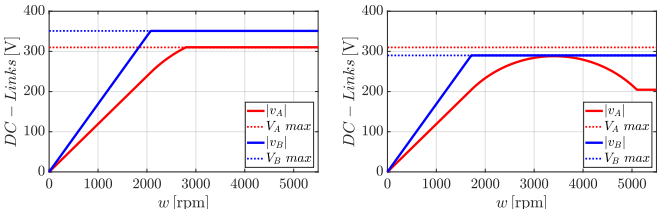


(a) (b)

Fig. 9: (a) Case 1: Voltage-versus-speed characteristic ideal DI for $VB = 351$ V. (b) Case 2: Voltage-versus-speed characteristic ideal DI for $VB = 290$ V.

evaluated by intersecting the current limit circle, (6) and (7) with both sides voltages saturated. The resulting intersection lays on the limit circle for current angle greater than $45°$.

The second flux-weakening region, denoted as 'Region C', is characterized by a decreasing power trend. This occurs either when both sides voltages are saturated or when the current angle reaches the MTPF trajectory. In such cases, the only viable solution to further increase the rotational speed involves reducing the magnitude of the current vector while keeping the current angle fixed [21].

In the next subsections, an analysis is conducted on the impact of FC voltage levels on torque-versus-speed characteristics, on voltage versus-speed-characteristics, and on the corresponding behavior on the $i_d$, $i_q$ plane. This examination encompasses two notable cases, each defined by distinct FC voltage levels.

### A. *First Case*

As described in [21], the condition and the limit to extend the base are the following:

$$\boldsymbol{v}_B \geq \boldsymbol{v}_A \frac{2\sqrt{\xi}}{1-\xi} \tag{10}$$

$$|\boldsymbol{v}_B| = |\boldsymbol{v}_A| \frac{L_d + L_q}{L_d - L_q} \tag{11}$$

where $\xi$ is the saliency ratio defined as $\xi = L_q/L_d$. The set-point value, $V_B$, is selected to be greater than (10) but less than (11). Opting for $V_B$ below (10) implies no increase in base speed compared to the SI case. Conversely, selecting $V_B$ higher than (11) indicates no further increase in base speed, but rather an extension of the flux-weakening region at a constant current module.

The first FC voltage level under study is chosen as $V_B = 351$ V as it corresponds to a value between (10) and (11). Fig. 8(a) shows the resulting torque versus speed characteristic (light green) of the DI configuration as well as the SI solution (dark green) [2]. It is notable that the base speed operation is extended with respect to the SI configuration, and the resulting electromagnetic torque is higher in flux weakening when the OEW configuration is adopted. As far as the voltage levels evolution over the rotational speed are concerned, it can be observed in Fig. 9(a) how the drive enters the flux weakening 'Region B' with the FC voltage level saturated and it stays saturated in the whole speed domain. The voltage versus speed characteristics shows that both $|v_A|$ and $|v_B|$ saturate during the flux weakening.

The corresponding current vector trajectories are represented in Fig. 7(a). In 'Region A', the trajectory followed is the ideal MTPA. Once the current limit circle has been intersected, corresponding to the base speed (i.e. $w_b^{DI} = 2076$ rpm), the current vector will be moved on the MTPV. The current vector angle shall not be increased further, otherwise $|v_A|$ would increase beyond the selected target fixed by the voltage source feeding the Main-Conv DC-link. Once the depowering speed is reached (i.e. $w_{dp}^{DI} = 2797$ rpm), both DC-links are saturated. The only feasible solution to further increase the rotational speed consists of decreasing the current vector magnitude. The drives will enter in 'Region C' and the DC-links modules will stay saturated in the whole speed domain.

### *B. Second Case*

The Second FC voltage level under study is chosen as $V_B = 290$ V as it corresponds to the value at which is intersected the MTPF trajectory between the two flux-weakening regions.

Fig. 8(b) compares the torque versus speed characteristic of the two DI cases. Compared to the previous case, it is notable that the constant torque region is less extensive (i.e. $w_b^{DI} = 1715$ rpm), while depowering speed (i.e. $w_{dp}^{DI} = 5100$ rpm) is higher than the first case. $w_{dp}^{DI}$ is reached when the corresponding current angle is $\theta_{dp} = tan^{-1}\frac{\overline{L}_d}{\overline{L}_q}$, and consequently the Main-Conv DC-link voltage level does not reach its target. Fig. 9(b) shows that $|v_A|$ in 'region B' does not saturate to its available maximum voltage. This behaviour can be explained by the fact that the d-current component, which is responsible for the most significant flux component (i.e. $\psi_d = \overline{L}_d i_d$), diminishes more significantly than the rate of increase of the q-current component after a certain angle. The voltage $v_A$ in Fig. 9(b) exhibits a peak, corresponding to the maximum torque per power factor (MTPPF). It was chosen to extend beyond this point for consistency with SI operations and to reach the MTPW, despite the decrease in maximum voltage.

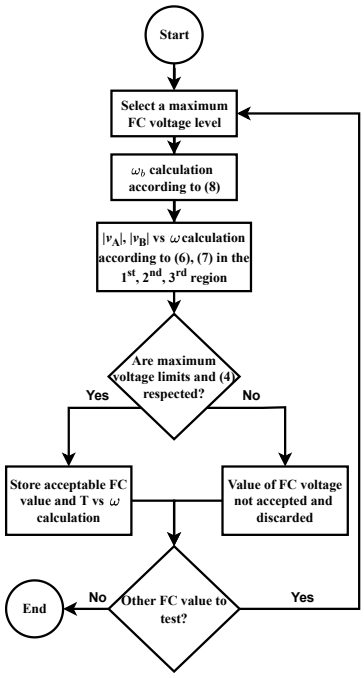


Fig. 10: Flowchart of the analytical approach to find the feasible $V_{FC}$ values for different operating regions.

## IV. Real OEW SyRel Motor Operations

The analytical analysis of the OEW SyRel model developed in the previous section remains valid even in the real case. The difference lies primarily in the non linearity (i.e. $L_d(i_d, i_q)$, $L_q(i_d, i_q)$), derived from the magnetic model outlined in Sec. II. The study is undertaken under the same hypothesis as III.

The identification of the three operating regions takes place based on the magnitudes of $|v_A|$ and $|v_B|$, along with the chosen trajectory of the current vector in the $dq$ plane. The three operational regions are based on the optimal operating trajectories of the machine under testing presented in Sec. II.

The base speed depends on the selected values of $V_B$. Fig. 12(a) illustrates the $V_B$ versus $w_b^{DI}$ characteristic. It is not possible to increase the base speed beyond a specific threshold (i.e. $w_{b,lim} = 2517$ rpm), that corresponds to (11). The limitation of the base speed results from the saturation of the DC link in the Main-Conv before the Aux-Conv for all values exceeding $w_{b,lim}$. Selecting the optimal operational curves of the machine under testing as the working trajectory renders the utilization of all $V_B$ values unfeasible. Fig. 12(a) illustrates the values of $V_B$ (cyan) that simultaneously comply with the constraints (4), (10), and the saturation of both DC links during operation within the three delineated regions. Fig. 10 shows the algorithm implemented to visualize the acceptable values

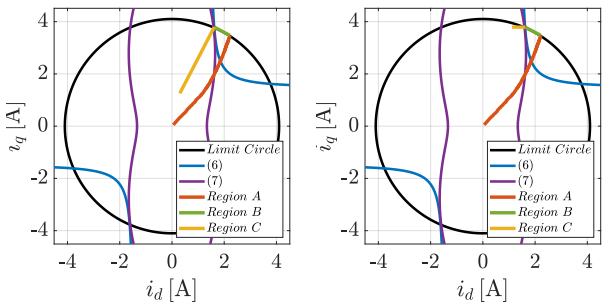


(a) (b)

Fig. 11: (a) Case 1: id,iq-plane Real DI trajectories. (b) Case 2: id,iq-plane Real DI trajectories.

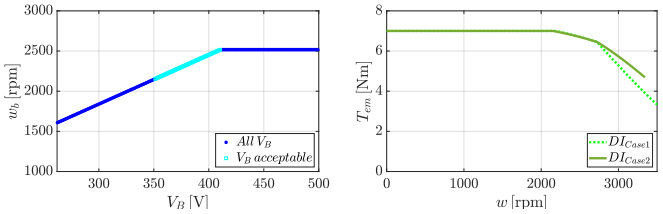


(a) (b)

Fig. 12: (a) Base Speeds value versus floating capacitor levels. (b) Torque-versus-speed characteristic real DI configurations.

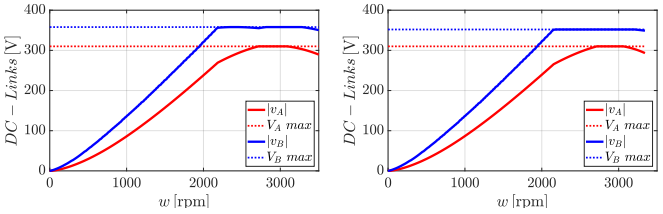


(a) (b)

Fig. 13: (a) Case 1: Voltage-versus-speed characteristic Real DI. (b) Case 2: Voltage-versus-speed characteristic Real DI.

of FC. Next sections will closely examine the results obtained from the steady state analysis, offering a detailed overview, and key findings and implications that emerged while studying the system under various operational conditions. Two cases will be presented, differing in the trajectory followed in 'Region C'. In the first case, starting from the depowering speed, the trajectory follows a path parallel to the MTPA curve. In the second case, the trajectory followed in the $dq$ plane is parallel to the d-axis. Fig.s 11(a) and 11(b) illustrate the two different possible paths.

### A. First Case

For the first scenario, the FC voltage level selected is $V_B = 351$ V. The chosen value is selected to lie between (10) and (11), as described in Sec. III.

Fig. 12(b) illustrates the resulting torque versus speed characteristic. It is evident that the behavior of the characteristic reflects that of the ideal case. In the real dual inverter configuration, the base speed is extended, and the depowering speed is reduced. The extension of the base speed results in the elongation of 'Region A'. Moreover, the torque in 'Region C' decreases exponentially as the trajectory followed is parallel to the MTPA. Adopting this trajectory involves employing an aggressive flux-weakening technique for the machine.

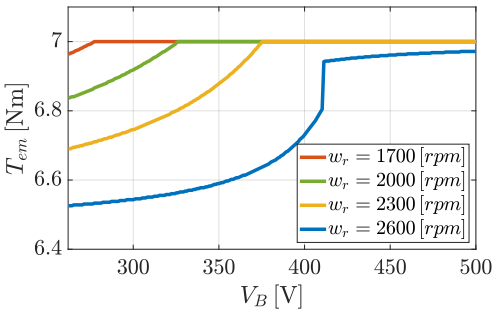


Fig. 14: Torque-versus-Voltage characteristic real DI configurations

Regarding the evolution of voltage levels over rotational speed, Fig. 13(a) shows that the system enters the flux weakening 'Region B' with a saturated FC voltage level, remaining saturated throughout the entire first field-weakening speed domain. However, in comparison to the ideal scenario depicted in Fig. 9(a), the two DC links do not remain saturated in 'Region C' but decrease, due to the implementation of the non-linear magnetic model. The voltage-speed characteristics indicate that both $|v_A|$ and $|v_B|$ saturate during the initial flux-weakening region. However, in the subsequent region, they only comply with the maximum voltage limit, differing from the ideal case.

The corresponding current vector trajectories are represented in Fig. 11(a). In 'Region A', the trajectory followed is the real MTPA. Once the current limit circle has been intersected, corresponding to the base speed (i.e. $w_b^{DI} = 2185$ rpm), the modules of the current vector is maintained constant and moved counterclockwise. The depowering speed is the one that performs the saturation of the Main-Conv. Once the depowering speed is reached (i.e. $w_{dp}^{DI} = 2720$ rpm), the trajectory selected is the one parallel to the MTPA. The objective is to pursue a trajectory similar to MTPW, one that, under (4) conditions, failed to meet the imposed constraints. Consequently, among the available alternatives, the decision is made to explore this possibility.

### B. Second Case

For the second scenario, the FC voltage level select is $V_B = 351$ V. Fig. 12(b) illustrates the resulting torque versus speed characteristic. It is noteworthy that there is a limit on the maximum machine speed following the trajectory parallel to the d-axis. This trajectory cannot be followed for all theoretical speeds because, beyond a certain speed limit (i.e. $w_{lim}^{DI} = 3104$ rpm), compliance with the imposed constraints on powers and voltages would be compromised. However, it is observed that in the second case, higher torque values are obtained for all possible speeds.

Regarding the evolution of voltage levels over rotational speed, Fig. 13(b) shows that the system enters the flux weakening 'Region B' with a saturated FC voltage level, remaining saturated throughout the entire field-weakening speed domain.

As in Fig. 13(a), similar results are observable in this case given the operation in the maximum voltage region. Small voltage differences can be appreciated, especially in the behaviour of $|v_B|$. Compared to the previous case, only $|v_A|$ decrease in 'Region C', that implies that, by following the trajectory parallel to the d-axis in the second flux weakening region, the DC-links of the system are utilized more efficiently, as the minimum DC link voltage is employed to meet the operational requirements within the desired operating point on the $T_{\text{em}}$ versus $\omega$ plane.

The current vector trajectories are illustrated in Fig. 11(b). In 'Region A,' the trajectory conforms to the actual MTPA. Upon intersecting the current limit circle, corresponding to the base speed (i.e. $w_b^{DI} = 2185$ rpm), the current vector is directed along the limit circle. Once the depowering speed is reached (i.e., $w_{dp}^{DI} = 2720$ rpm), the chosen path for the second scenario follows a trajectory parallel to the d-axis. The selected current trajectory aims to reach the MTPW. However, to adhere to (4) constraints and due to a significant decline in voltage $V_A$, the trajectory was terminated before reaching the MTPW.

At least, the electromagnetic torque variations were examined across different $V_B$ values at four rotational speeds (i.e. $\omega_r = 1700$ rpm, $\omega_r = 2000$ rpm, $\omega_r = 2300$ rpm, $\omega_r = 2600$ rpm), and the results are depicted in Fig. 14. Notably, voltage values ensuring the machine avoids entering the flux weakening region were identified for the initial three speeds. Consequently, to optimize torque output at a given speed, it is recommended to choose a voltage value on the FC that sustains machine operation within the constant torque region. Furthermore, maintaining the same voltage value, operating at lower rotational speeds is advised, as it results in higher generated torque. For the fourth considered speed, flux weakening is observed across all $V_B$ values, leading to lower generated torque in all instances.

In conclusion, the analysis of the real machine yields significant insights. The base speed of the machine under testing has been extended in the dual inverter configuration. Furthermore, till the maximum speed of the real machine (i.e. $w_{max} = 2500$ rpm), all conditions are met. This encompasses adherence to power constraints (4) and voltage constraints, highlighting the robust performance and compliance of the system, even in demanding operational scenarios.

## V. Experimental Results

The experimental setup is depicted in Fig. 15. The picture shows the test bench, consisting of the measuring instruments and the inverters (ocher and cyan), which feed the open-end winding SyRel motor (red) coupled with a PMSM (yellow) acting as load. Inverter A is based on a SiC power module (BSM180D12P2C101) by Rohm, inverter B is based on a SiC power module (CAS120M12BM2) by Cree, whereas inverter C is based on an insulated gate bipolar transistor (IGBT) power module (FF400R12KT3IGBT) developed by Infineon. The switching frequency is 20 kHz. The commutation dead-time of inverter C is 2 $\mu$s, while the commutation dead-time

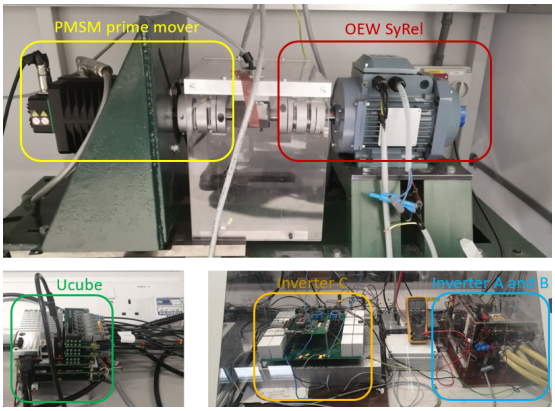


Fig. 15: SyRel test rig.

of inverter A and B is 1 $\mu$s. The control board is the uCube system (green) designed at the University of Nottingham [24]. The parameters of the drive are the same as shown in Table I. The measured signals have been acquired, transferred to a PC, and plotted via Matlab. The analysis is centered on steady-state conditions, and the adopted control scheme is presented in [5]. The DC-Link voltage is fixed at 580 V, while the speed is set by the prime mover at 1900 and 2000 rpm for two separate cases. Fig. 16(a) and 17(a) show the waveform of the phase A reference voltage vector of inverters A and B, in the stationary reference frame. Fig. 16(b) and 17(b) depict the phase A current of the machine and the reference voltage of inverter A at a mechanical speed of 1900 and 2000 rpm, respectively. As can be seen, the stator current exhibits sinusoidal characteristics and is in phase with the reference voltage of inverter A, conforming to the expected unity power factor. Similarly, the waveform of the measured voltage of inverter B is sinusoidal, and it leads the voltage waveform of inverter A by 90°. Fig. 16(c) and 17(c) illustrate the $dq$-current reference tracking at steady state for a nominal torque of the SyRel Machine, as presented in Fig. 6(a). The FC voltages reference tracking are depicted in Fig. 16(c) and 17(c) and their values permit the unity power factor for the machine under testing. It is noteworthy how the reference values align with those obtained through mathematical analysis in Section IV. The differences lie in the fact that in the mathematical model, the stator resistance is not considered, and additionally, a safety factor is taken into account for control purposes [5].

In conclusion, the primary objective of the developed drive is to expand the speed range and enhance the power factor of SyRel machines in SI configuration. The DI system enables an extension of the base speed guaranteeing a unity power factor for the whole torque-versus-speed characteristic. In the flux weakening regions, where the power factor of a single inverter drive rapidly diminishes and its active power diminishes to zero, the power factor of the dual inverter drive remains constant. Unfortunately, the behavior under these operating conditions cannot be evaluated, as this speed range (i.e., $\omega > 2500$ rpm) exceeds the maximum speed attainable by the drive.

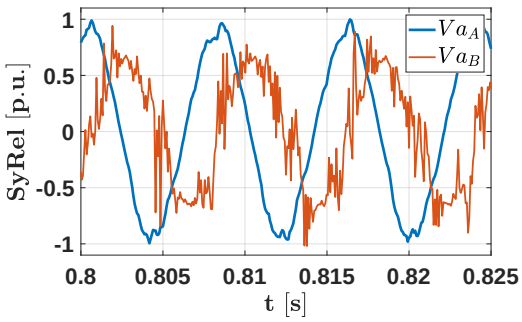


(a)

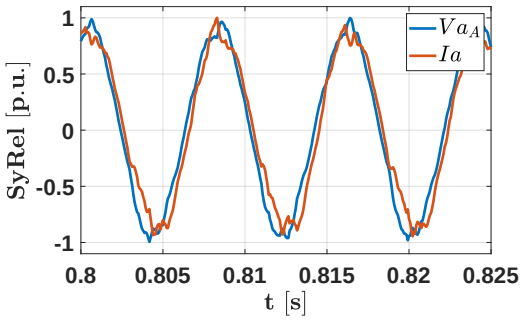


(b)

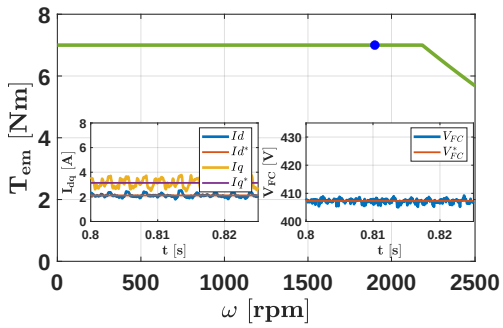


(c)

Fig. 16: Experimental results at 1900 rpm at steady-state. (a) Voltage references waveform of phase A for inverter A and inverter B. (b) Voltage reference waveform and measured current of phase A for inverter A. (c) Torque-versus-speed characteristic with $dq$-current reference tracking and $V_{FC}$ reference tracking.

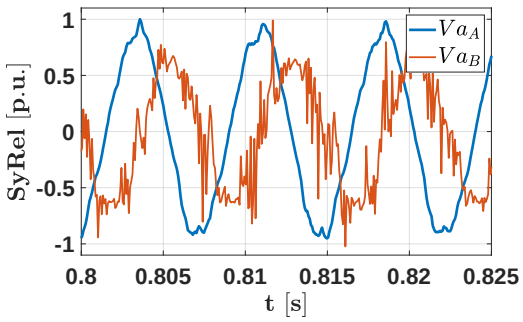


(a)

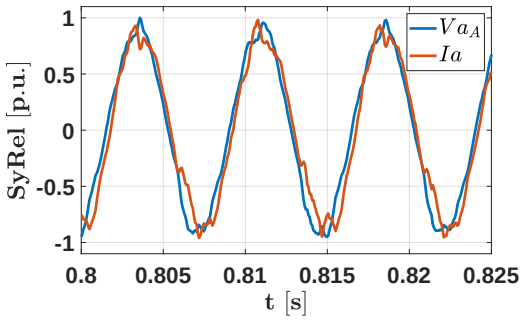


(b)

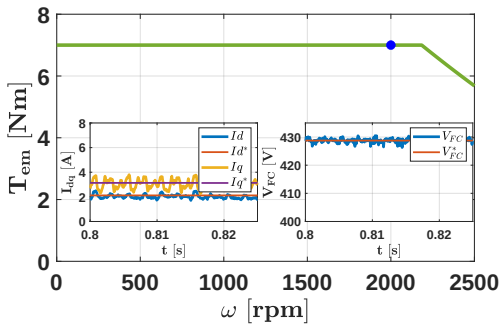


(c)

Fig. 17: Experimental results at 2000 rpm at steady-state. (a) Voltage references waveform of phase A for inverter A and inverter B. (b) Voltage reference waveform and measured current of phase A for inverter A. (c) Torque-versus-speed characteristic with $dq$-current reference tracking and $V_{FC}$ reference tracking.

## VI. Discussions

The benefit of using a DI drive over a SI architectures resides in the enhanced torque-versus-speed characteristics along with the unity power factor operation. Similar torque-versus-speed operation enhancement would be achieved by increasing the voltage rating of the main bridge converter. If the voltage rating of the converter is doubled, the base speed is proportionally extended, along with the constant torque region. This study has primarily focused on low-voltage AC drives, which typically do not operate with DC links exceeding 800 V. Similar results to the ones achieved in this manuscript in terms of torque-versus-speed capability can be achieved by upgrading the DC-link voltage. However, this is a high-cost solution given that the voltage class of the semiconductors must be upgraded to at least 1.7 kV. Additionally, the motor's insulation class would also need to be upgraded accordingly. Furthermore, no power factor compensation could be achieved by means of upgrading the inverter ratings to boost the torque-versus-speed capability of the drive. The analysis provided was focused on the unity power factor operation. Nevertheless, the constraint on the reactive power of the Main-Conv can be relaxed to achieve enhanced torque-versus-speed operations with respect to the case study at the cost of a reduced power factor of the main bridge [17]. This is the object of a future investigation to introduce a further degree of freedom to shape

the drive-operation according to the specific requirement of the application.

## VII. Conclusion

This paper presents an in-depth analysis of a OEW SyRel motor drive system. The investigation focuses on the impact of the floating capacitor voltage level on torque versus speed characteristics, considering both ideal and real scenarios. The use of a dual-inverter setup addresses challenges such as low power factor and limited constant power speed range in SyRel drives. The experimental identification and description of the machine's magnetic model are presented, providing crucial insights into the non-linear flux versus current characteristics of the SyRel motor. The analytical models of the SyRel drive system in SI and DI configurations are presented, emphasizing the three operational regions based on current vector trajectories. The analysis is extended to real scenarios, considering non-linear inductances. In conclusion, the experimental results are presented underling the extension of the base speed and the compliance with all constraints.

## Acknowledgement

This work was supported by the Marie Skłodowska-Curie Actions (MSCA) under the European Union's Horizon 2020 Research and Innovation Staff Exchange (RISE) under Grant 872001.

## References

[1] M. Murataliyev, M. Degano, M. Di Nardo, N. Bianchi, and C. Gerada, "Synchronous reluctance machines: A comprehensive review and technology comparison," *Proc. IEEE*, vol. 110, no. 3, pp. 382–399, 2022.

[2] N. Bianchi, S. Bolognani, E. Carraro, M. Castiello, and E. Fornasiero, "Electric vehicle traction based on synchronous reluctance motors," vol. 52, no. 6, pp. 4762–4769, 2016.

[3] B. Ban, S. Stipetić, and M. Klanac, "Synchronous reluctance machines: Theory, design and the potential use in traction applications," in *2019 International Conference on Electrical Drives  Power Electronics (EDPE)*, pp. 177–188, 2019.

[4] B. Poudel, E. Amiri, P. Rastgoufard, and B. Mirafzal, "Toward less rare-earth permanent magnet in electric machines: A review," *IEEE Transactions on Magnetics*, vol. 57, no. 9, pp. 1–19, 2021.

[5] A. Amerise, L. Rovere, A. Formentini, M. Mengoni, L. Zarri, and P. Zanchetta, "Electric drive based on an open-end winding surface PM synchronous machine with a floating capacitor bridge," pp. 2709–2718, 2020.

[6] V. Oleschuk, "Strategies, schemes, and algorithms of synchronous space-vector pwm for voltage source inverters of open-end winding motor drives: An overview," in *2021 International Conference on Electromechanical and Energy Systems (SIELMEN)*, pp. 069–075, 2021.

[7] Y. Zuo, X. Zhu, X. Si, and C. H. T. Lee, "Fault-tolerant control for multiple open-leg faults in open-end winding permanent magnet synchronous motor system based on winding reconnection," vol. 36, no. 5, pp. 6068–6078, 2021.

[8] L. Rovere, A. Formentini, G. L. Calzo, P. Zanchetta, and T. Cox, "IGBT-SiC dual fed open end winding PMSM drive," in *2017 IEEE International Electric Machines and Drives Conference (IEMDC)*, pp. 1–7, 2017.

[9] M. Zerdani, S. A. E. M. Ardjoun, H. Chafouk, and M. Denaï, "Experimental investigation of decoupled discontinuous pwm strategies in open-end winding induction motor supplied by a common dc-link," *IEEE Journal of Emerging and Selected Topics in Power Electronics*, vol. 11, DOI 10.1109/JESTPE.2023.3258799, no. 3, pp. 3087–3096, 2023.

[10] J. Kalaiselvi and S. Srinivas, "Bearing currents and shaft voltage reduction in dual-inverter-fed open-end winding induction motor with reduced CMV PWM methods," vol. 62, no. 1, pp. 144–152, 2015.

[11] E. L. Soares, C. B. Jacobina, N. B. de Freitas, N. Rocha, A. C. N. Maia, and A. M. N. Lima, "A multilevel open-end winding six-phase induction motor drive topology based on three two-level three-phase inverters," *IEEE Transactions on Industry Applications*, vol. 59, DOI 10.1109/TIA.2023.3291354, no. 5, pp. 6360–6372, 2023.

[12] L. Rovere, G. Valente, A. Formentini, and P. Zanchetta, "Parameters and volt–ampere ratings of a floating capacitor open-end winding synchronous motor drive for extended CPSR," vol. 69, no. 5, pp. 4576–4586, 2022.

[13] S. Chowdhury, P. W. Wheeler, C. Patel, and C. Gerada, "A multilevel converter with a floating bridge for open-end winding motor drive applications," vol. 63, no. 9, pp. 5366–5375, 2016.

[14] L. Rovere, A. Formentini, G. L. Calzo, P. Zanchetta, and T. Cox, "Zero-sequence voltage elimination for dual-fed common dc-link open-end winding pmsm high-speed starter–generator—part i: Modulation," *IEEE Transactions on Industry Applications*, vol. 55, no. 6, pp. 7804–7812, 2019.

[15] X. Yuan, C. Zhang, and S. Zhang, "Torque ripple suppression for open-end winding permanent-magnet synchronous machine drives with predictive current control," vol. 67, no. 3, pp. 1771–1781, 2020.

[16] L. Wang, W. Huang, and F. Bu, "The reduction of zero-sequence voltage for open-end winding asynchronous motor driver with dual inverter," in *2017 20th International Conference on Electrical Machines and Systems (ICEMS)*, pp. 1–5, 2017.

[17] M. Mengoni, A. Amerise, L. Zarri, A. Tani, G. Serra, and D. Casadei, "Control scheme for open-ended induction motor drives with a floating capacitor bridge over a wide speed range," *IEEE Transactions on Industry Applications*, vol. 53, DOI 10.1109/TIA.2017.2704910, no. 5, pp. 4504–4514, 2017.

[18] C. Perera, G. J. Kish, and J. Salmon, "Decoupled floating capacitor voltage control of a dual inverter drive for an open-ended winding induction motor," *IEEE Transactions on Power Electronics*, vol. 35, DOI 10.1109/TPEL.2019.2955412, no. 7, pp. 7305–7316, 2020.

[19] Y.-F. Jia, N. Xu, L. Chu, Y. Zhang, Z. Xu, Y.-K. Li, and Z.-H. Yang, "Control strategy for an open-end winding induction motor drive system for dual-power electric vehicles," *IEEE Access*, vol. 8, DOI 10.1109/ACCESS.2020.2964105, pp. 8844–8860, 2020.

[20] A. D. Kiadehi, K. El Khamlichi Drissi, and C. Pasquier, "Adapted NSPWM for single DC-link dual-inverter fed open-end motor with negligible low-order harmonics and efficiency enhancement," vol. 31, no. 12, pp. 8271–8281, 2016.

[21] J. Riccio, L. Rovere, S. Odhano, M. Di Nardo, and P. Zanchetta, "Model-predictive control of open-end winding synchronous reluctance motor drives," in *2022 IEEE Energy Conversion Congress and Exposition (ECCE)*, pp. 1–8, 2022.

[22] J. Riccio, P. Karamanakos, S. Odhano, M. Tang, M. D. Nardo, G. Tresca, and P. Zanchetta, "Modulated model-predictive integral control applied to a synchronous reluctance motor drive," *IEEE Journal of Emerging and Selected Topics in Power Electronics*, vol. 11, no. 3, pp. 3000–3010, 2023.

[23] E. Armando, R. I. Bojoi, P. Guglielmi, G. Pellegrino, and M. Pastorelli, "Experimental identification of the magnetic model of synchronous machines," vol. 49, no. 5, pp. 2116–2125, 2013.

[24] A. Galassini, G. Lo Calzo, A. Formentini, C. Gerada, P. Zanchetta, and A. Costabeber, "ucube: Control platform for power electronics," in *2017 IEEE Workshop on Electrical Machines Design, Control and Diagnosis (WEMDCD)*, pp. 216–221, 2017.

**Jacopo Riccio** (Member, IEEE) received his B.Sc. and M.Sc. degrees in Mechanical Engineering from the University of Roma Tre, Rome, Italy, in 2014 and 2018, respectively. He completed his Ph.D. in Electrical Engineering at the University of Nottingham, UK, in 2023. Since 2023, Dr. Riccio has been a Research Fellow with the same group at the University of Nottingham. His research interests include the control of electric drives, particularly model-based predictive control and sensorless algorithms, as well as experimental characterization of internal permanent magnet and synchronous reluctance machines. He was honored with the best IEEE-IAS Prize Paper Award in 2024.

**Filippo Gemma** (Student Member, IEEE) received the B.Sc. and M.Sc degrees in electrical engineering in 2020 and 2022, respectively, from the University of Pavia, Pavia, Italy, where he is currently working toward the Ph.D. degree in electrical engineering with the PELAB, the Power Electronics group at the University of Pavia. His research interests include multilevel and reconfigurable converters for automotive applications, and control of electric drives based on model-based predictive control.

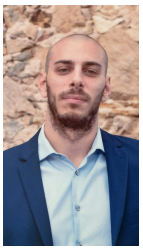

**Luca Rovere** (Member, IEEE) received the M.S. degree with honours in Electrical Engineering from the University of Genova in 2015. Before graduating he spent a period at the Power Electronics and Machine Control Group of the University of Nottingham working on predictive controllers and sensorless control techniques. In 2019 he received the Ph.D. in Electrical and Electronic engineering from the University of Nottingham. In 2019 he became a Research Fellow at the same University. In 2020 he joined TTPI, as a Power Electronics Engineer. His research interests include control and modulations for electrical drives and the modelling, design and optimization of power electronics converters.

**Giulia Tresca** (Member, IEEE) received her B.Sc. degree in Electrical Engineering from the University of L'Aquila, Italy, in 2015. She completed her M.Sc. and Ph.D. degrees in Electrical Engineering at the University of Pavia, Italy, in 2017 and 2023, respectively. From 2017 to 2019, she worked as a Test Engineer at Infineon in Villach, Austria. She is currently an Assistant Professor at PELAB, the Power Electronics Laboratory at the University of Pavia. Her research interests include multilevel and reconfigurable converters for automotive applications, battery management systems, and control of electrical drives.

**Shafiq Odhano** (S'13–M'15–SM'20) received the M.Sc. degree in electrical engineering and the Ph.D. degree in power electronics, machines, and drives from the Politecnico di Torino, Turin, Italy, in 2014. He has been affiliated with the Politecnico di Torino as a postdoctoral research fellow and with the University of Nottingham, UK, as a research fellow. He is currently a lecturer in electric drives at Newcastle University, Newcastle Upon Tyne, UK. His research interests include high-performance control of servo-drives, model predictive control of power converters, multiphase machines and drives, and self-commissioning of three-phase and multiphase ac motor drives.

**Mauro Di Nardo** (M'18) received the M.Sc. (Hons.) degree in electrical engineering from the Polytechnic University of Bari, Italy, in 2012, and the Ph.D. degree in electrical machine design from the University of Nottingham, U.K., in 2017. From 2017 to 2019, he was with the AROL spa leading the R&D team focusing on electrical drives design for mechatronics applications. Between 2019 and 2023, he was with the Power Electronics and Machine Control Group of the University of Nottingham as Research Fellow. He is currently an assistant professor in electrical machine and drives at the Polytechnic University of Bari, Italy. He serves as an Associate Editor for the IEEE Open Journal of Industry Applications and IEEE Transactions on Energy Conversion.

**Michele Degano** (M'15, SM'21) received his Master's degree in Electrical Engineering from the University of Trieste, Italy, in 2011, and his Ph.D. degree in Industrial Engineering from the University of Padova, Italy, in 2015. Between 2014 and 2016, he was a post-doctoral researcher at The University of Nottingham, UK. In 2016 he was appointed Assistant Professor in Advanced Electrical Machines, at The University of Nottingham, UK. He was promoted Associate Professor in 2020 and Professor in 2022 leading research projects for the development of future hybrid electric aerospace platforms and electric transports. He is author/co-author of more than 150 scientific papers. Within the Power Electronics, Machines and Control (PEMC) Research Institute, his main research focuses on electrical machines and drives for industrial, automotive, railway and aerospace applications, ranging from small to large power. He is currently the Chief Engineer of Nottingham Drives Specialist Services (NDSS), the University of Nottingham business unit dedicated to support the industrialisation of electrical machines and drives.

**Pericle Zanchetta** (M '00, SM '15, F '19) received his MEng degree in Electronic Engineering and his Ph.D. in Electrical Engineering from the Technical University of Bari (Italy) in 1993 and 1997 respectively. In 1998 he became Assistant Professor of Power Electronics at the same University. In 2001 he became lecturer in the PEMC research group at the University of Nottingham – UK, where he became Professor in Control and Power Electronics in 2013. From 2022 he is full professor of Power Electronics at the University of Pavia, Italy and part time professor at the University of Nottingham. He has published over 400 peer reviewed scientific papers. Professor Zanchetta is member of the board of directors of the IEEE Industry Application Society (IAS) and Editor in Chief of the IEEE Open Journal of Industry Applications since 2020; he is IEEE-IAS Education Department chair since 2023. He has been vice-chair and Chair of the IEEE IAS Industrial Power Conversion Systems Department (2018-2021) and secretary, vice chair and Chair of the IEEE IAS Industrial Power Converters Committee (2012-2017). His research interests include control and optimization of power converters and drives, Matrix and multilevel converters.